Applied Surface Science 364 (2016) 651–659

Contents lists available at ScienceDirect

Applied Surface Science

journal homepage: www.elsevier.com/locate/apsusc

Tailored lithium storage performance of graphene aerogel anodes with controlled surface defects for lithium-ion batteries

Hui Shan[a,1], Dongbin Xiong[a,1], Xifei Li[a,*], Yipeng Sun[b], Bo Yan[a], Dejun Li[a,*], Stephen Lawes[c], Yanhua Cui[d,*], Xueliang Sun[c,a]

[a] Energy & Materials Engineering Centre, College of Physics and Materials Science, Tianjin Normal University, Tianjin 300387, China
[b] College of Polymer Science and Engineering, Sichuan University, Chengdu 610065, China
[c] Nanomaterials and Energy Lab, Department of Mechanical and Materials Engineering, Western University, London, Ontario N6A 5B9, Canada
[d] Institute of Electronic Engineering, CAEP, Mianyang 621900, China

ARTICLE INFO

Article history:
Received 28 August 2015
Received in revised form
10 December 2015
Accepted 18 December 2015
Available online 29 December 2015

Keywords:
Hydrothermal self-assembly
Graphene aerogel
Defects
Lithium ion batteries
Anode materials

ABSTRACT

Three dimensional self-assembled graphene aerogel (GA) anode materials with some surface defects have been successfully generated through a facile hydrothermal procedure using graphene oxide as precursor. The morphologies and textural properties of as-obtained GA were investigated by scanning electron microscopy, transmission electron microscopy, X-ray photoelectron spectroscopy, Raman and other spectroscopy techniques. The surface defects and electrical conductivities of GA can be controlled by adjusting the hydrothermal reaction time. The results indicate that GA with a reaction time of 6 h exhibits extremely high reversible capacity (1430 mAh g^{-1} at the current density of 100 mA g^{-1}) and superior rate capability (587 mAh g^{-1} at 800 mA g^{-1}) with excellent cycling stability (maintaining a reversible capacity of 960 mAh g^{-1} at 100 mA g^{-1} after 100 cycles). It is demonstrated that the 3D porous network with increased defect density, as well as the considerable electrical conductivity, results in the excellent electrochemical performance of the as-made GA anodes in lithium-ion batteries.

1. Introduction

Graphene, a two-dimensional (2-D) nanostructure of carbon, has received particular attention over the past decade in various fields due to its characteristic properties, such as high mechanical strength, large surface area, superior electrical conductivity, and strong chemical stability [1–6]. Recently, it has become one of the most exciting research topics in lithium-ion batteries (LIBs) [7–10]. It is considered a potential substitute material to replace commercial graphite anodes, which exhibit a inferior theoretical specific capacity of 372 mAh g^{-1} and poor rate performance, and thus hardly satisfy the changing requirements of portable electronic devices as well as recently developed electric vehicles [11,12].

The theoretical capacity of graphene can reach up to 744 mAh g^{-1} (twice as much as that of graphite) due to the fact that both sides of a graphene sheet can accommodate two Li ions, in each hexagonal loop of carbon (Li_2C_6) [13,14]. However, aggregation due to the π–π stacking interaction limits lithium ion insertion/extraction and the permeation of electrolyte [15], which reduces the electrochemical performance when using bare graphene as an anode material. As a result, some attention has been focused on increasing the reversible capacity of graphene anodes by diverse treatments, such as heteroatom doping [16–18] and defect formation [19,20]. For example, our previous work demonstrated that nitrogen doping of graphene significantly enhanced its cycling performance [16]. Guo's group developed the nitrogen-doped graphene with a nitrogen content range of 3.95–6.61% and their results indicated that the nitrogen content in graphene has a significant impact on the lithium storage performance [21]. In addition to electrical conductivity, the performance improvement can be attributed to defect formation in the nitrogen-doped graphene anode. Similarly, as previously reported by our group, increased surface defects on graphene positively affect its electrochemical performance in LIBs [16]. For instance, the defect sites introduced into graphene provide more Li^+ storage electrochemically active sites and contribute to increasing the specific capacity. Therefore, the surface defects of graphene anodes have a great influence on their lithium storage capability.

In this study, we present a facile hydrothermal method combined with freeze drying to convert graphene oxide into graphene aerogels (GAs) with porous three-dimensional structures. More

* Corresponding authors.
E-mail addresses: xfli2011@hotmail.com (X. Li), dejunli@mail.tjnu.edu.cn (D. Li), cuiyanhua@netease.com (Y. Cui).
[1] These authors contributed equally to this work.

http://dx.doi.org/10.1016/j.apsusc.2015.12.143
0169-4332/

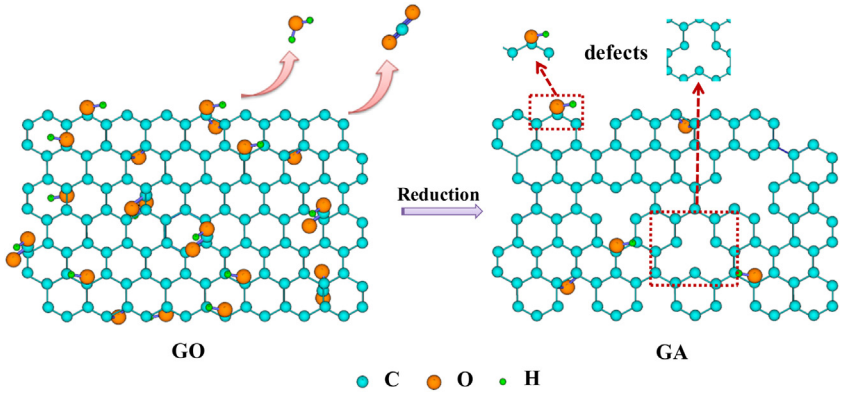

Scheme 1. Schematic illustration showing the formation of graphene aerogel (GA) with defects.

importantly, by controlling the reaction time we were able to tailor the surface defects of GA. The effects of the GA surface defects on lithium storage were investigated in detail. The results indicate that GA with more surface defects exhibit superior energy capacity and good cycling stability. It is expected that this study will make significant contributions to the further development of graphene anodes for LIBs.

2. Experimental

2.1. Materials

Graphite powder (purity ≥ 99.95%), with particle diameters of no more than 1.3 μm (see Fig. S1), was obtained from the Aladdin Chemistry Co., Ltd. (Shanghai, China). Other chemicals, including $KMnO_4$ (99%), $NaNO_3$ (99%), concentrated sulfuric acid (95–98%), hydrochloric acid (36–38%), and H_2O_2 (30%) were supplied by Tianjin FengChuan Chemical Reagent Technology Ltd. (China). All of the chemicals were of analytical reagent grade and used as received without further purification.

2.2. Synthesis of graphite oxide (GO)

GO was synthesized from flake graphite by a modified Hummers' method following the procedure reported by our group [22]. In a typical synthesis, 1.0 g of graphite and 0.75 g of $NaNO_3$ were first mixed with 34 mL of H_2SO_4 (98%) in a 250 mL breaker, and the mixture was then stirred for 2 h in an ice water bath. Meanwhile, 4.5 g of $KMnO_4$ was slowly added into the breaker under vigorous stirring while maintaining the solution temperature below 10 °C. The resultant mixture was then stirred at room temperature for 5 days, followed by the addition of 100 mL of 5% concentrated sulfuric acid with vigorous stirring for 2 h. After that, a moderate amount of H_2O_2 was added into the mixture until no gas bubbles were produced and the color changed to brilliant yellow. Then the resultant graphite oxide was repeatedly washed with HNO_3 (10%) aqueous solution and deionized (DI) water several times. Finally, the resulting GO was then thoroughly centrifuged with deionized water until pH = 7 and the product were dried at room temperature for 24 h.

2.3. Synthesis of graphene aerogel (GA)

Various GA samples were obtained through a hydrothermal procedure by controlling the reaction time. In a typical experiment, the resultant dry GO was dispersed in water by ultrasonication for 30 min to make a GO aqueous dispersion (3 mg mL^{-1}). The obtained brown dispersion was then centrifuged for 30 min at 10,000 rpm to remove large aggregates. Then the as-prepared dispersions were

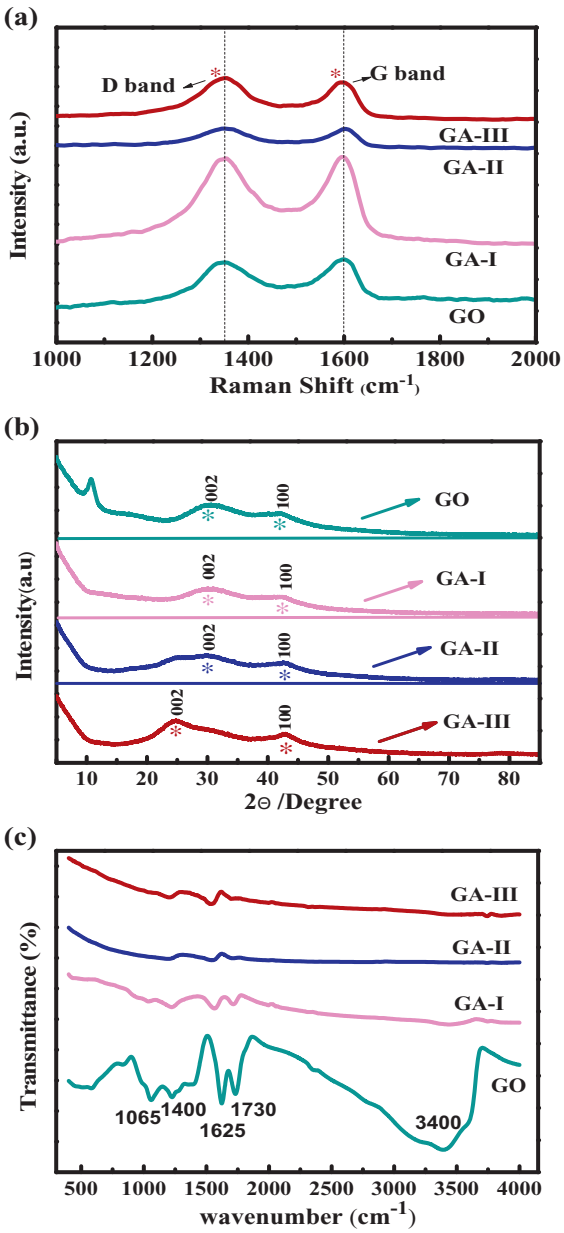

Fig. 1. (a) Raman spectra of GO, GA-I, GA-II and GA-III; (b) XRD patterns of GO, GA-I, GA-II and GA-III; (c) FTIR spectra of GO, GA-I, GA-II and GA-III.

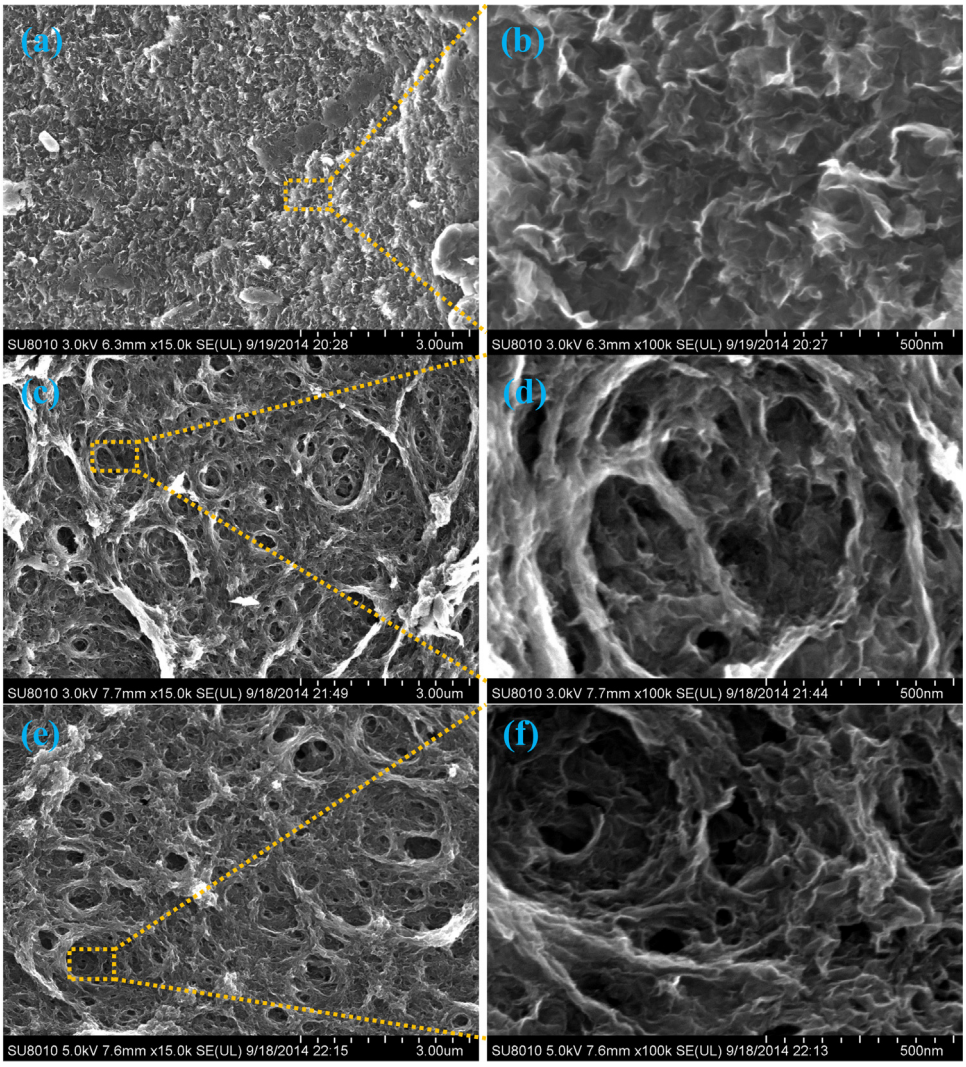

Fig. 2. SEM images of GA-I (a, b), GA-II (c, d), and GA-III (e, f).

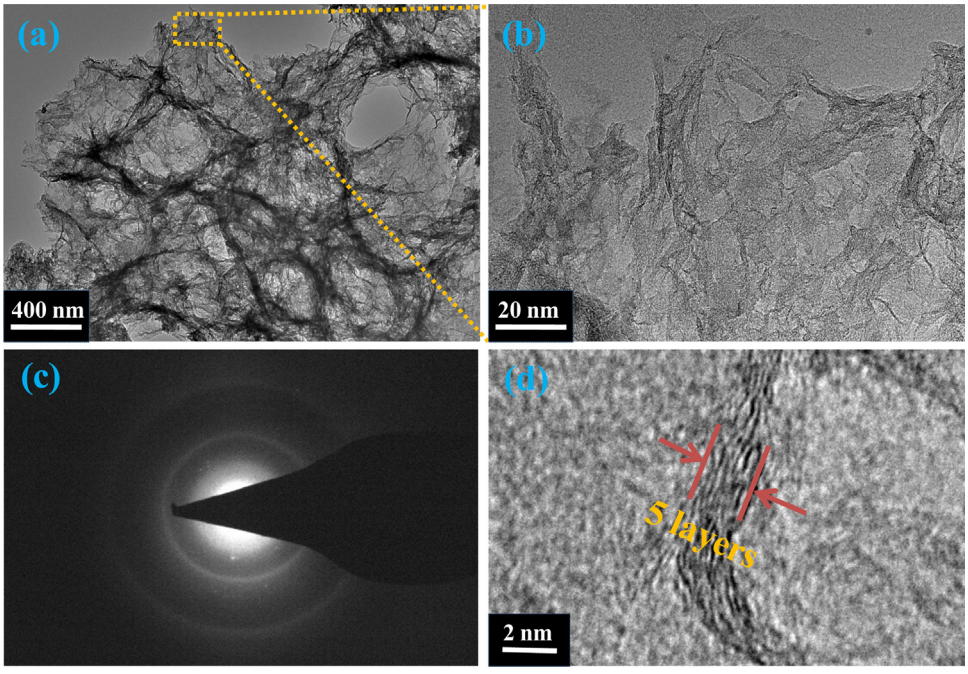

Fig. 3. TEM images of GA-II (a, b, d). Inset of (c) is the corresponding electron diffraction pattern of GA-II.

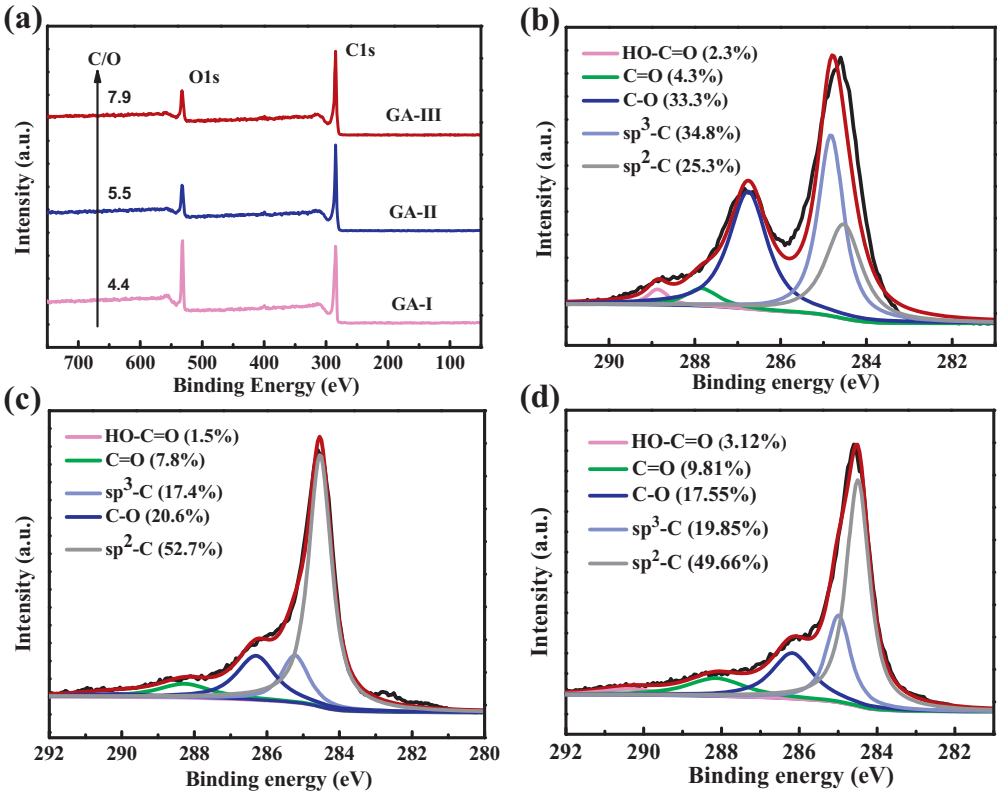

Fig. 4. (a) The broad XPS spectra of GA-I, GA-II and GA-III; C 1s spectra of (b) GA-I, (c) GA-II and (d) GA-III.

transferred into a Teflon-lined autoclave with 50 mL capacity and hydrothermally treated at 180 °C for 1, 6, and 12 h, and then the obtained graphene hydrogel was freeze-dried to obtain a graphene aerogel (GA). The materials with hydrothermal reaction times of 1, 6, and 12 h were labeled as GA-I, GA-II, and GA-III, respectively.

2.4. Materials characterization

The powder XRD patterns of the samples were recorded with an X-ray diffractometer (D8 Advance of Bruker, Germany) using Cu/Kα radiation in the range from 5° to 85°. The Raman measurement of as-synthesized materials was conducted on a confocal Micro Raman Spectrometer with LabRAM HR800 system (HORIBA, Korea) in the range of 1000–2000 cm^{-1}. The FT-IR spectra were recorded on an IRAffinity-1 FT-IR spectrometer (Shimadzu), and the specimens for FT-IR measurement were prepared by grinding the dried powder with KBr and then compressing into thin pellets. XPS was performed on a VG ESCALAB MK II X-ray photoelectron spectrometer. The elemental composition of the samples was also analyzed by energy dispersive X-ray spectroscopy (EDX, INCAx-sight, Oxford). The morphologies of the samples were verified using field-emission scanning electron microscopy (FE-SEM, SU8010, Hitachi) and high-resolution transmission electron microscopy (HR-TEM, JEM-3000F).

2.5. Electrochemical characterization

The electrochemical behavior of the as-prepared GA samples was investigated employing CR2032 coin-type cells, lithium serving as the counter and reference electrode. In a typical experiment, the working electrodes are prepared by mixing 80 wt% active materials (GA), 10 wt% polyvinylidenefluoride (PVDF) binder and 10 wt% acetylene black (Super-P) dispersed in N-methyl-2-pyrrolidinone (NMP). Then the mixture was subsequently cast on copper foil and dried under vacuum at 90 °C for 12 h. The coin cells were assembled in a glove box filled with high purity argon. The electrolyte used was 1 M $LiPF_6$ dissolved in a solvent consisting of 50% dimethyl carbonate and 50% ethylene carbonate by volume. The electrode performance was measured by galvanostatic discharge–charge employing a battery test station (LANHE CT2001A) in a voltage range from 0.01 to 3.0 V (vs. Li/Li^+). Cyclic voltammetry (CV) was performed using the Princeton Applied Research VersaSTAT 4 at a scan rate of 0.1 mV s^{-1} in the potential window of 0.01–3.0 V (vs. Li/Li^+). Electrochemical impedance spectroscopy (EIS) tests were measured on the Princeton Applied Research VersaSTAT 4 between a frequency range from 0.01 Hz to 100 kHz with AC amplitude of 5.0 mV.

3. Results and discussion

A schematic illustration of the fabrication procedure for graphene aerogels (GAs) is depicted in Scheme 1. Hydrothermal method was employed to reduce the Hummers' GO. During the reduction process, oxygen functional groups were lost by the way of H_2O and CO_2, resulting in the formation of vacancies, edges and some remaining oxygen functional groups on the surface of the graphene. Porous GA with many surface defects was obtained from the reduced products via a freeze-drying process. The hydrothermal reaction time significantly affects the species and amounts of surface defects such as vacancies, edges and some remaining oxygen functional groups. As a result, the surface defects of GA could be tailored by controlling hydrothermal reaction time, resulting in various GA with different reduction degree.

Raman spectra were examined to characterize as-prepared GA samples, as shown in Fig. 1(a). All samples exhibit two peaks positioned at about 1350 and 1585 cm^{-1}, respectively. G-band symbolizes the performance characteristics of graphitic layers, and D band corresponds to the defective graphitic structure or disordered

Table 1
C species content (at%) of the samples based on XPS results.

Samples	sp^2—C	sp^3—C	C—O	C=O	HO—C=O
GA-I	25.3	34.8	33.3	4.3	2.3
GA-II	52.7	17.4	20.6	7.8	1.5
GA-III	49.66	19.85	17.55	9.81	3.12

carbon [23,24]. The disorder induced by the graphite amorphization results in an increased relative intensity ratio (I_D/I_G) of the D to G bands, following the reduction of the sp^2 domain size [5,25]. The I_D/I_G value of the GO, GA-I, GA-II, and GA-III was 1.36, 1.80, 2.08 and 2.00, respectively. The increasing I_D/I_G ratio of GA was due to the introduction of more edge sites and defects such as vacancies and bonding disorders in the graphene lattice. Herein, the highest I_D/I_G ratio of GA-II implies that it contains the most sp^3 bonds and defects, which results in a significant variation in the electronic structure, as supported by its electrochemical performance.

XRD patterns of the as-synthesized materials were measured to better clarify the structure. Fig. 1(b) shows a comparison of the XRD patterns of GO, GA-I, GA-II, and GA-III. As shown in Fig. 1(b), a typical diffraction peak of GO at 11.8° is observed, which can be assigned to the (002) reflection of GO, corresponding to an interlamellar spacing of about 0.749 nm. The interlamellar spacing of GO increases in comparison with that of natural graphite (see Fig. S2, the natural graphite is distinguished by the peak appears at 26.6°, corresponding to an interlamellar spacing of 0.34 nm) because of the presence of intercalated H_2O molecules and various oxygen-containing groups such as —COOH, —OH and —O— during the oxidation process [6]. Importantly, the broad (002) diffraction angles of GA-I, GA-II, and GA-III gradually increase to 24.8°, 26.9°, and 29.2°, respectively, after hydrothermal treatment. It is attributed to a decrease in the interlamellar distance because of the decrease in surface functional groups and intercalated H_2O molecules. Clearly, by adjusting the hydrothermal reaction time, the interlayer distance and the content of remaining oxygen functional groups can be controlled.

The FT-IR spectra of GO, GA-I, GA-II, and GA-III are shown in Fig. 1(c). It is obvious that the FT-IR spectrum of GO shows strong characteristic peaks at 1065, 1400, 1625, and 1730 cm^{-1}, which are ascribe to the vibration of C—O bonds, C—O deformation, adsorbed water, and C=O stretching, respectively. In addition, the broader peak around 3400 cm^{-1} is corresponded to O—H stretching [26]. These confirm the presence of the oxygen-containing groups (C—O—C, —COOH, —OH) on the surface of GO. In contrast, a new weak absorption band was observed at 1564 cm^{-1}, attributed to the aromatic skeletal C=C stretching vibration of GA [27]. Only weak absorption bands at 1400 and 1730 cm^{-1} in the FT-IR spectrum of GA-I and 1400 cm^{-1} in the FT-IR spectra of GA-II and GA-III were observed, indicating the partial elimination of oxygen functional groups from GO and the formation of some conjugated regions in GA. It can be also concluded that the amount of oxygen-containing groups decline as the hydrothermal reaction time increases.

SEM was performed to investigate the morphologies and microstructures of the GA materials. As shown in Fig. 2, the typical corrugated graphene is composed of ultrathin layered platelets at both low magnification (Fig. 2(a), (c) and (e)) and high magnification (Fig. 2(b), (d) and (f)). Differing from the morphology of ultrathin and small layered platelets for GA-I (Fig. 2(a) and (b)), GA-II (Fig. 2(c) and (d)) and GA-III (Fig. 2(e) and (f)) show an interconnected framework of ultrathin graphene nanosheets with a porous structure. The twisted nanosheets are overwritten with each other randomly to structure a network with micropores interpenetrating inside and thus the GA-II and GA-III have 3D structures, similar to previous reports [28,29]. Clearly, the hydrothermal reaction time makes a difference to the morphology and microstructure of the GA.

TEM was used for further observation of the typical structures of GA materials. As shown in Figs. 3 and S3, GA-II (Fig. 3(a)) and GA-III (Fig. S3(c)) both exhibit a morphology of highly transparent gossamer sheets with some micropores visible, as previously reported in the literatures [3,30]. The transparent gossamer structure was observed in the high magnification image (Figs. 3(b) and S3(d)), while there was not an obvious porous structure for GA-I (Fig. S3(a) and (b)), which is in agreement with the SEM results. The resultant SAED pattern, as shown in Fig. 3(c), displays ring patterns without defined diffraction spots, suggesting that the obtained GA-II had a multi-layer structure with structural irregularity due to the remaining oxygen functional groups on the surface of the self-assembled GA and other defects, such as vacancies and bonding disorders in the graphene lattice, caused by the reduction process [31]. In Fig. 3(d), the HRTEM image of GA-II confirms the multi-layered structure. The larger interlayer distance and increased number of structural defects of self-assembled GA compared to GO will contribute to the enhanced electrochemical performance when employed as anode material for LIBs.

X-ray photoelectron spectroscopy (XPS), an important technique to provide information about the elemental composition and chemical state of GA samples, has been taken for further analysis. Surface functional groups on the GA samples could be derived from XPS measurements. As shown in Fig. 4(a), the two distinct peaks at about 286 and 533 eV are related to C and O, respectively. Moreover, the atomic ratio of carbon to oxygen (C/O) varies with the reaction time, and the atomic ratio is in the following order: GA-I (4.4) < GA-II (5.5) < GA-III (7.9), indicating that the oxygen functional groups of the samples gradually decrease along with the extension of hydrothermal reaction time. As previously reported [32], a lower oxygen content leads to a higher electrical conductivity. Based on the high resolution C 1s XPS analysis (Fig. 4(b), (c) and (d)), five types of C species exist in GA samples. The peaks centered at 288.7, 287.5 and 286.6 eV may be assigned to the carboxyl groups (COOR), carbonyl groups (C=O) and epoxy groups (C—O) [33,34], respectively. The peaks positioned at 285.2 and 284.5 eV can be attributed to sp^3 and sp^2 carbon [35], respectively. It can be seen from Table 1 and Fig. 4(b), (c) and (d) that there exists a remarkable decrease in the epoxy-group content and a slight increase in carbonyl-group content of GA-II and GA-III compared with that of GA-I, resulting in the decrease in oxygen content. The graphitic carbon content of GA samples is significantly increased due to the hydrothermal reduction of GO. Furthermore, the decrease in oxygen content and the formation of defects may improve the electrical conductivity, and provide more lithium ions insertion/extraction active sites for GA, which will lead to a significant improvement in the reversible capacity and rate capability.

The electrochemical properties of the as-prepared GA anodes were studied by cyclic voltammetry measurements. Fig. 5(a)–(c) shows the CV curves of GA-I, GA-II, and GA-III electrodes conducted at a voltage range of 0.01–3.0 V (vs. Li^+/Li) and at a scan rate of 0.1 mV s^{-1}. As shown in Fig. 5(a), a typical peak close to 0 V was observed due to the lithium-ion intercalation into the carbon anode. The curve profile from 0.5 to 0.01 V in the second and third cycles is weaker than that in the first cycle, originating from some fading of active Li^+ storage sites due to GA aggregation during charge/discharge processes [36]. As for the CV profiles of GA-II and GA-III electrodes in Fig. 5(b) and (c), a prominent peak located at about 0.6 V in the first cycle is mainly related to the formation of solid-electrolyte-interphase (SEI) film on the surface of the anode. This peak disappears in subsequent cycles due to the stable existence of SEI.

The discharge–charge behavior of the GA-I, GA-II, and GA-III electrodes at a constant current density of 100 mA g^{-1} between 0.01

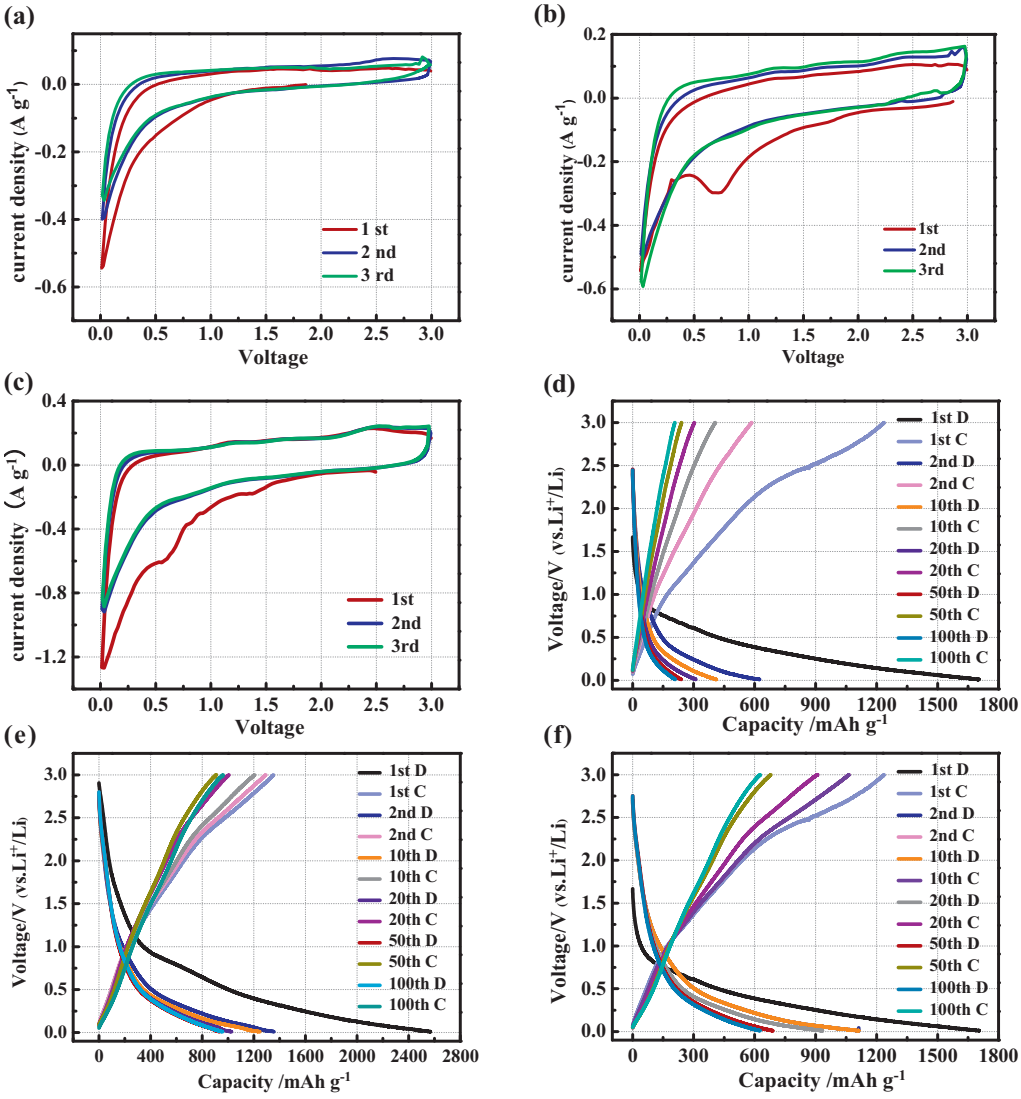

Fig. 5. Cyclic voltammograms of (a) GA-I, (b) GA-II, and (c) GA-III in the voltage range of 0.01–3 V (vs. Li/Li^+) at a scanning rate of 0.2 mV s^{-1}; galvanostatic discharge–charge profile of (d) GA-I, (e) GA-II, and (f) GA-III at the current rate of 100 mA g^{-1} in the voltage range of 0.01–3 V (vs. Li/Li^+).

and 3 V is shown in Fig. 5(d)–(f). The discharge–charge curves of all GA samples in the 1st, 2nd, 10th, 20th, 50th, and 100th cycles exhibited a similar lithium storage process. The discharge–charge curves with no obvious potential plateaus indicate the existence of electrochemically and geometrically non-equivalent lithium storage sites within the GA anodes, as reported in our previous study [22]. The initial discharge capacity of GA-II is 2566 mAh g^{-1}, which is higher than that of GA-I (1670 mAh g^{-1}) and GA-III (1718 mAh g^{-1}). In the second charge–discharge process, GA-I and GA-III delivered reversible capacities of 687 and 1065 mAh g^{-1}, respectively, while a higher reversible capacity of 1440 mAh g^{-1} was obtained by GA-II. For these three GA samples, the extra capacity beyond that of the theoretical value may be attributed to the additional edges and defects for Li^+ storage, and the irreversible capacity loss in the first cycle can be attributed to the formation of SEI. The as-obtained high reversible capacities of GA-II and GA-III anodes might be related to the porous structure and the increased interlayer distance between graphene nanosheets [8], as well as the formation of a large number of defects. The slight performance fading may be due to inactivate Li^+ storage sites [8,36,37].

The cycling stabilities of GO, GA-I, GA-II, and GA-III are shown in Fig. 6(a), which were conducted at a current density of 100 mA g^{-1}. Obviously, GO showed a poor cycling stability with a reversible capacity of no more than 100 mAh g^{-1} due to very poor electrical conductivity. In contrast, GA-I displayed an increased cycling performance with a discharge capacity of 209 mAh g^{-1} in the 100th cycle, when GO was treated by hydrothermal reaction for a short time, but the obtained performance is still poor. With the increase of hydrothermal reaction time, GA-II and GA-III strongly enhanced cycling performance with high discharge capacities of 954 and 769 mAh g^{-1} after 100 cycles, respectively. It is obvious that the hydrothermal reaction time significantly affects the anode performance. The GA-II electrode exhibited the highest reversible capacity and most stable cycling performance among the three GA anodes. Additionally, as shown in Figs. 6(a) and S4, all GA anodes displayed almost 100% coulombic efficiency, illustrating that the obtained GA materials as anodes for LIBs exhibit outstanding cycling stability.

The rate capabilities of GA-I, GA-II, and GA-III electrodes at various charge/discharge rates are shown in Fig. 6(b). Both GA-II and GA-III displayed elevated capacities and superior stability at each current density in comparison to GA-I. Moreover, the discharge capacities of GA-II are always higher than that of GA-III under the same current density. For example, at a current

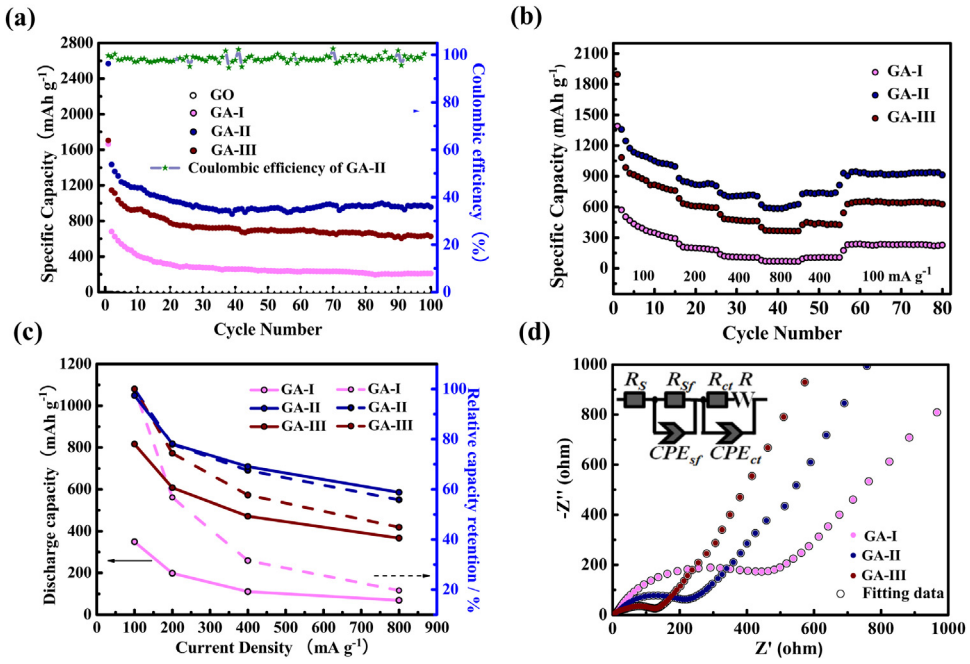

Fig. 6. (a) Cycling performance of GO, GA-I, GA-II and GA-III up to 100 cycles at a current density of 100 mA g^{-1} and coulombic efficiency of GA-II; (b) rate performance of GA-I, GA-II and GA-III at various current densities; (c) capacity retention of GA-I, GA-II and GA-III at different current density; (d) Nyquist plots of GA-I, GA-II and GA-III after 10 cycles at a charge state (3.0 V) and the corresponding simulation results (inset is the equivalent circuit used to simulate an experimental curve).

density of 100 mA g^{-1}, the GA-II can be reversibly charged to 1052 mAh g^{-1}. When the current density was increased to 200, 400 and 800 mA g^{-1}, the corresponding reversible capacities for GA-II are stabilized at 823, 717, and 587 mAh g^{-1}, respectively. What's more, a specific capacity of 922 mAh g^{-1} can be recovered and stabilized when the current density is returned to the initial current density (100 mA g^{-1}). These results further confirm the importance of the porous structure, electrical conductivity, and defect sites. Fig. 6(c) displays the discharge capacities of the 5th cycle at various current densities and relative capacity retention compared with the capacity at 100 mA g^{-1}. Among the three GA samples, GA-II was found to show higher capacity retention at 200, 400, and 800 mA g^{-1} compared to the GA-I and GA-III anodes, indicating that GA-II possesses outstanding rate capability in LIB performance.

Electrochemical impedance spectroscopy (EIS) studies of the GA-I, GA-II, and GA-III electrodes in the full charged state (3.0 V) after 10 cycles were performed to determine the influence of oxygen content on the electrical conductivity, and the Nyquist plots are presented in Fig. 6(d). It presents one capsuled semicircle in the high to medium frequency ranges, which relate to the charge transfer resistance (R_{ct}), and a line in the low-frequency range, which can be considered as Warburg impedance (ZW) associated with the lithium ion diffusion in the bulk of the active materials [18,38]. An equivalent circuit was employed to simulate the impedance spectra, as shown in the inset of Fig. 6(d), where R_s represents the resistance of the electrolyte, R_{sf} and CPE_{sf} are the resistance and capacitance of the SEI formed on the electrodes, respectively. R_{ct} and CPE_{ct} are the charge-transfer resistance and double-layer capacitance, respectively, W is the Warburg impedance in correlation with the diffusion of lithium ions into the bulk electrodes [39,40]. Using the equivalent circuit, the fitting values are presented in Table 2. It can be expressly noted that after 10 cycles the charge transfer resistance (R_{ct}) values of GA-I, GA-II, and GA-III are 452.6, 227 and 113.6 Ω, respectively. This indicates that the decreased oxygen content in GA results in the decrease of charge transfer resistance and enhancement of electronic conductivity. The R_{sf} value of GA-II (6.44 Ω) is relatively lower compared to that of GA-I (9.07 Ω) and GA-III (20.8 Ω), which may contribute to enhancing the electrochemical performance of GA-II.

Table 2
The typical fitted parameters in the electrochemical impedance spectroscopy.

Samples	R_{sf}	R_{ct}	CPE_{sf}	CPE_{ct}
GA-I	9.1	452.6	1.62E−05	1.65E−05
GA-II	6.4	227.0	7.12E−05	5.35E−05
GA-III	20.8	113.6	1.34E−05	9.98E−05

This remarkable difference in the electrochemical performance among the materials could be the result of the various amounts of defects and different electrical conductivity. As illustrated in Scheme 2, abundant edges, randomly distributed vacancies and residual oxygen functional groups exist on GA, providing more active sites for Li storage and facilitating the transfer of Li ions and electrons in the anode materials during charge/discharge processes, for instance, some vacancies originating from residual oxygen functional groups would be beneficial for the adsorption of Li ions, and the vacancies in the graphene lattice may facilitate the vertical transfer of Li ions, resulting in high capacity and outstanding rate capability. More importantly, plethoric oxygen content will result in poor electrical conductivity, as illustrated by the EIS results. Thus, the optimized tradeoff of the defects and electrical conductivity will be necessary, which suggests that the GA sample with considerable defects and acceptable electrical conductivity shows a higher reversible capacity as an anode material for LIBs.

In present work, by regulating the hydrothermal time, the reduction degree, species and amounts of surface defects can be well controlled, for instance, as demonstrated by Raman and XPS results, increasing reaction time leads to the enhance of defects involved in edge sites, vacancies and bonding disorders but the decrease of oxygen functional groups. As a result, under an appropriate treatment time, GA-II exhibited a high reversible capacity and excellent high-rate capability when employed as anode material for Li-ion batteries, which was considered to benefit from the

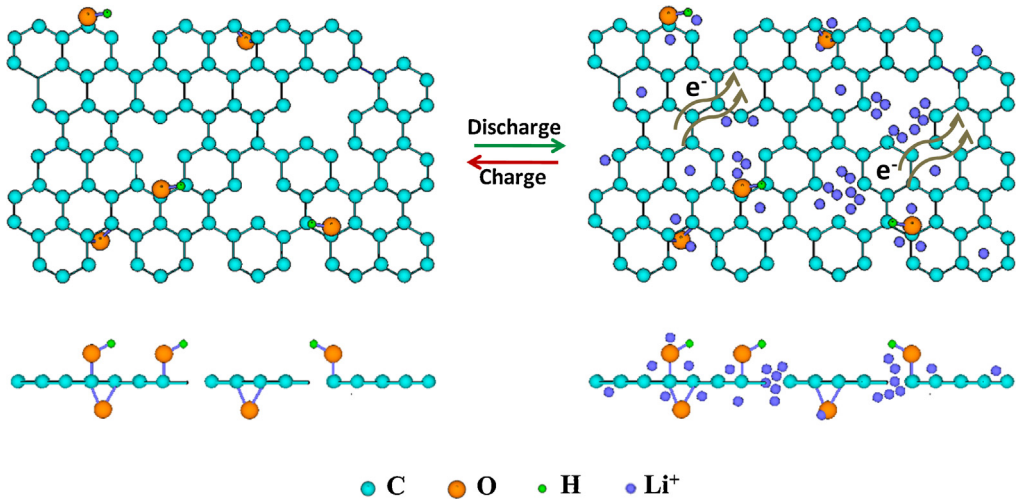

Scheme 2. Schematic illustration for the lithium-storage mechanism of graphene aerogel (GA) with defects.

abundant lithium storage sites and fast diffusion of lithium ions with a low ion-transport resistance.

On the basis of the aforementioned discussion, it is clear that GA-II with a hydrothermal reaction time of 6 h demonstrated the best electrochemical performance. The enhanced electrochemical performance of GA-II is due to combined functions of the specific porous structure, high specific surface area, acceptable electronic conductivity, and surface defects such as the remaining oxygen-containing functional groups and the vacancies in the graphene lattice. The large number of defects and high specific surface area result in more sites available for Li^+ adsorption. The porous structure also allows for easier access of the electrolyte to the electrode surface and therefore efficient electron and ion transfer into the electrodes. This results in the improved electrochemical performance of GA-II, making this material highly attractive as a promising anode material in LIBs.

4. Conclusion

In summary, we have developed a facile hydrothermal approach to synthesize self-assembled 3D GA for use as high-capacity anode materials in LIBs. A series of characterization and analysis indicates that the high capacity, excellent electrochemical stability, and rate capability are attributed to the unique structure (porosity, defect sites, etc.) and high electronic conductivity. The importance of defects on enhancing the capacity and electrochemical stability of the GA anode was demonstrated. Moreover, the surface defects can be easily tailored by controlling the reaction time. It is believed that this study opens the door to further increase the electrochemical performance of graphene anodes for LIBs.

Acknowledgements

This research was supported by the National Natural Science Foundation of China (51572194), the Key Projects of Tianjin Municipal Natural Science Foundation of China (14JCZDJC32200 and 13JCZDJC33900), the Project 2013A030214 supported by CAEP (China Academy of Engineering Physics), LPMT (Laboratory of Precision Manufacturing Technology), CAEP (KF14006 and ZZ13007), Academic Innovation Funding of Tianjin Normal University (52XC1404), Training Plan of Leader Talent of University in Tianjin and the program of Thousand Youth Talents in Tianjin of China.

Appendix A. Supplementary data

Supplementary material related to this article can be found, in the online version, at http://dx.doi.org/10.1016/j.apsusc.2015.12.143.

References

[1] K.S. Subrahmanyam, S.R.C. Vivekchand, A. Govindaraj, C.N.R. Rao, A study of graphenes prepared by different methods: characterization, properties and solubilization, J. Mater. Chem. 18 (2008) 1517.
[2] S. Yang, X. Feng, S. Ivanovici, K. Mullen, Fabrication of graphene-encapsulated oxide nanoparticles: towards high-performance anode materials for lithium storage, Angew. Chem. Int. Ed. 49 (2010) 8408–8411.
[3] Y. Bai, R.B. Rakhi, W. Chen, H.N. Alshareef, Effect of pH-induced chemical modification of hydrothermally reduced graphene oxide on supercapacitor performance, J. Power Sources 233 (2013) 313–319.
[4] L. Cui, Y. Liu, X. He, Iron(II) tetraaminophthalocyanine functionalized graphene: synthesis, characterization and their application in direct methanol fuel cell, J. Electroanal. Chem. 727 (2014) 91–98.
[5] G. Tang, Z.-G. Jiang, X. Li, H.-B. Zhang, A. Dasari, Z.-Z. Yu, Three dimensional graphene aerogels and their electrically conductive composites, Carbon 77 (2014) 592–599.
[6] H.-M. Ju, S.H. Huh, S.-H. Choi, H.-L. Lee, Structures of thermally and chemically reduced graphene, Mater. Lett. 64 (2010) 357–360.
[7] Y. Hu, X. Li, D. Geng, M. Cai, R. Li, X. Sun, Influence of paper thickness on the electrochemical performances of graphene papers as an anode for lithium ion batteries, Electrochim. Acta 91 (2013) 227–233.
[8] D. Cai, S. Wang, L. Ding, P. Lian, S. Zhang, F. Peng, H. Wang, Superior cycle stability of graphene nanosheets prepared by freeze-drying process as anodes for lithium-ion batteries, J. Power Sources 254 (2014) 198–203.
[9] W. Ai, Z. Du, Z. Fan, J. Jiang, Y. Wang, H. Zhang, L. Xie, W. Huang, T. Yu, Chemically engineered graphene oxide as high performance cathode materials for Li-ion batteries, Carbon 76 (2014) 148–154.
[10] Q. Fan, L. Lei, X. Xu, G. Yin, Y. Sun, Direct growth of $FePO_4$/graphene and $LiFePO_4$/graphene hybrids for high rate Li-ion batteries, J. Power Sources 257 (2014) 65–69.
[11] H. Buqa, D. Goers, M. Holzapfel, M.E. Spahr, P. Novák, High rate capability of graphite negative electrodes for lithium-ion batteries, J. Electrochem. Soc. 152 (2005) A474.
[12] J.B. Goodenough, Y. Kim, Challenges for rechargeable Li batteries, Chem. Mater. 22 (2010) 587–603.
[13] N.A. Kaskhedikar, J. Maier, Lithium storage in carbon nanostructures, Adv. Mater. 21 (2009) 2664–2680.
[14] B. Luo, L. Zhi, Design and construction of three dimensional graphene-based composites for lithium ion battery applications, Energy Environ. Sci. (2014).
[15] X. Ma, G. Ning, Y. Sun, Y. Pu, J. Gao, High capacity Li storage in sulfur and nitrogen dual-doped graphene networks, Carbon 79 (2014) 310–320.
[16] X. Li, D. Geng, Y. Zhang, X. Meng, R. Li, X. Sun, Superior cycle stability of nitrogen-doped graphene nanosheets as anodes for lithium ion batteries, Electrochem. Commun. 13 (2011) 822–825.
[17] Z. Jiang, Z.-J. Jiang, X. Tian, L. Luo, Nitrogen-doped graphene hollow microspheres as an efficient electrode material for lithium ion batteries, Electrochim. Acta 146 (2014) 455–463.

[18] H. Wang, C. Zhang, Z. Liu, L. Wang, P. Han, H. Xu, K. Zhang, S. Dong, J. Yao, G. Cui, Nitrogen-doped graphene nanosheets with excellent lithium storage properties, J. Mater. Chem. 21 (2011) 5430.
[19] M. Terrones, A.R. Botello-Méndez, J. Campos-Delgado, F. López-Urías, Y.I. Vega-Cantú, F.J. Rodríguez-Macías, A.L. Elías, E. Muñoz-Sandoval, A.G. Cano-Márquez, J.-C. Charlier, Graphene and graphite nanoribbons: morphology, properties, synthesis, defects and applications, Nano Today 5 (2010) 351–372.
[20] H. Wang, C. Zhang, Z. Liu, L. Wang, P. Han, H. Xu, K. Zhang, S. Dong, J. Yao, G. Cui, Nitrogen-doped graphene nanosheets with excellent lithium storage properties, J. Mater. Chem. 21 (2011) 5430–5434.
[21] H.-L. Guo, P. Su, X. Kang, S.-K. Ning, Synthesis and characterization of nitrogen-doped graphene hydrogels by hydrothermal route with urea as reducing-doping agents, J. Mater. Chem. A 1 (2013) 2248–2255.
[22] X. Li, Y. Hu, J. Liu, A. Lushington, R. Li, X. Sun, Structurally tailored graphene nanosheets as lithium ion battery anodes: an insight to yield exceptionally high lithium storage performance, Nanoscale 5 (2013) 12607–12615.
[23] A.C. Ferrari, J.C. Meyer, V. Scardaci, C. Casiraghi, M. Lazzeri, F. Mauri, S. Piscanec, D. Jiang, K.S. Novoselov, S. Roth, A.K. Geim, Raman spectrum of graphene and graphene layers, Phys. Rev. Lett. 97 (2006).
[24] A.C. Ferrari, Raman spectroscopy of graphene and graphite: disorder, electron–phonon coupling, doping and nonadiabatic effects, Solid State Commun. 143 (2007) 47–57.
[25] S. Ye, J. Feng, P. Wu, Highly elastic graphene oxide-epoxy composite aerogels via simple freeze-drying and subsequent routine curing, J. Mater. Chem. A 1 (2013) 3495–3502.
[26] Z. Jiang, X. Zhao, Y. Fu, A. Manthiram, Composite membranes based on sulfonated poly(ether ether ketone) and SDBS-adsorbed graphene oxide for direct methanol fuel cells, J. Mater. Chem. 22 (2012) 24862–24869.
[27] A. Hu, X. Chen, Q. Tang, Z. Liu, B. Zeng, One-step synthesis of Fe_3O_4@C/reduced-graphite oxide nanocomposites for high-performance lithium ion batteries, J. Phys. Chem. Solids 75 (2014) 588–593.
[28] Z.S. Wu, A. Winter, L. Chen, Y. Sun, A. Turchanin, X. Feng, K. Mullen, Three-dimensional nitrogen and boron co-doped graphene for high-performance all-solid-state supercapacitors, Adv. Mater. 24 (2012) 5130–5135.
[29] P. Chen, J.-J. Yang, S.-S. Li, Z. Wang, T.-Y. Xiao, Y.-H. Qian, S.-H. Yu, Hydrothermal synthesis of macroscopic nitrogen-doped graphene hydrogels for ultrafast supercapacitor, Nano Energy 2 (2013) 249–256.
[30] L. Jiang, Z. Fan, Design of advanced porous graphene materials: from graphene nanomesh to 3D architectures, Nanoscale 6 (2014) 1922–1945.
[31] J. Wang, H.S. Wang, K. Wang, F.B. Wang, X.H. Xia, Ice crystals growth driving assembly of porous nitrogen-doped graphene for catalyzing oxygen reduction probed by in situ fluorescence electrochemistry, Sci. Rep. 4 (2014) 6723.
[32] K. Krishnamoorthy, M. Veerapandian, K. Yun, S.J. Kim, The chemical and structural analysis of graphene oxide with different degrees of oxidation, Carbon 53 (2013) 38–49.
[33] C. Hu, X. Zhai, L. Liu, Y. Zhao, L. Jiang, L. Qu, Spontaneous reduction and assembly of graphene oxide into three-dimensional graphene network on arbitrary conductive substrates, Sci. Rep. 3 (2013) 2065.
[34] M. Ye, Z. Dong, C. Hu, H. Cheng, H. Shao, N. Chen, L. Qu, Uniquely arranged graphene-on-graphene structure as a binder-free anode for high-performance lithium-ion batteries, Small 10 (2014) 5035–5041.
[35] H.R. Byon, B.M. Gallant, S.W. Lee, Y. Shao-Horn, Role of oxygen functional groups in carbon nanotube/graphene freestanding electrodes for high performance lithium batteries, Adv. Funct. Mater. 23 (2013) 1037–1045.
[36] J. Zhang, Z. Xie, W. Li, S. Dong, M. Qu, High-capacity graphene oxide/graphite/carbon nanotube composites for use in Li-ion battery anodes, Carbon 74 (2014) 153–162.
[37] F. Zheng, Y. Yang, Q. Chen, High lithium anodic performance of highly nitrogen-doped porous carbon prepared from a metal-organic framework, Nat. Commun. 5 (2014) 5261.
[38] K. Zhang, H. Wang, X. He, Z. Liu, L. Wang, L. Gu, H. Xu, P. Han, S. Dong, C. Zhang, J. Yao, G. Cui, L. Chen, A hybrid material of vanadium nitride and nitrogen-doped graphene for lithium storage, J. Mater. Chem. 21 (2011) 11916.
[39] B. Yan, M. Li, X. Li, Z. Bai, L. Dong, D. Li, Electrochemical impedance spectroscopy illuminating performance evolution of porous core–shell structured nickel/nickel oxide anode materials, Electrochim. Acta 164 (2015) 55–61.
[40] C. Wang, Z. Guo, W. Shen, Q. Xu, H. Liu, Y. Wang, B-doped carbon coating improves the electrochemical performance of electrode materials for Li-ion batteries, Adv. Funct. Mater. 24 (2014) 5511–5521.